EES Catalysis

PAPER

View Article Online
View Journal

Cite this: DOI: 10.1039/d5ey00312a

Tailoring penta-coordinated aluminium species on silica–alumina *via* flame spray pyrolysis for enhanced arene benzylation

Xingxu Liu, [a] Wenjie Yang,[a] Luke A. O'Dell, [b] Haipeng Li,[cd] Qinfen Gu, [e] Suman Pokhrel, *[cdf] Lutz Mädler *[cdf] and Jun Huang *[a]

Received 31st October 2025,
Accepted 27th November 2025

DOI: 10.1039/d5ey00312a

rsc.li/eescatalysis

Flame spray pyrolysis (FSP) was employed to tailor the coordination environment of aluminum species on amorphous silica–alumina (ASA) for enhanced solid acidity. By regulating the oxygen flow, the formation of penta-coordinated Al (Al^V) species was promoted, especially the surface-distorted Al^Vb type. Advanced solid-state NMR and XAS analyses confirmed that Al^V species incorporate into the silica network and interact with nearby silanol groups to form strong Brønsted acid sites (BASs) through pseudo-bridging structures. The resulting ASA catalysts exhibited increased acid strength, with TMPO-^{31}P NMR shifts up to 67 ppm, comparable to zeolite-like acidity. These structural features correlate with significantly improved catalytic activity and selectivity in arene benzylation. This study establishes a clear synthesis–structure–acidity–function relationship and offers a rational strategy for designing high-performance ASA-based solid acids.

Broader context

The sustainable transformation of chemicals and fuels requires replacing corrosive liquid acids, such as HF and H_2SO_4, with environmentally benign and recyclable solid acids. However, controlling the strength and density of acid sites in solid materials remains a major challenge. This study introduces a scalable flame spray pyrolysis method to tailor the coordination of aluminium species on amorphous silica–alumina, generating highly active penta-coordinated Al sites that form strong Brønsted acidity comparable to zeolites. The resulting catalysts enable efficient benzylation of arenes under mild, solvent-free conditions. Beyond this specific reaction, the strategy provides a general framework for designing solid acids with tunable acidity, bridging the gap between conventional silica–alumina and zeolitic materials. This approach offers both environmental and economic benefits by enabling cleaner, safer, and energy-efficient pathways for sustainable chemical manufacturing.

1. Introduction

Silicon- and aluminum-based mixed oxides like amorphous silica–alumina (ASA) have become pivotal in modern catalysis due to their moderate and strong Brønsted acid sites (BASs) generated by the aluminium species in the silica network, making them versatile solid acids in various chemical processes.[1,2] In addition to Brønsted acidity, ASA also provides Lewis acid sites (LASs) formed by unsaturated aluminum species, which can initiate reactions requiring electron-pair acceptors, like alcohol dehydration.[3–5] LASs are also present and contribute significantly to the overall catalytic activity and selectivity of ASAs. The interplay between LASs and BASs enables a synergistic effect, optimizing reaction pathways and enhancing product yields.[6–8] ASA is also widely used as an acid support for metal nanoparticles, enabling unconstrained mass transfer and delivering bi-functional catalytic performance due to the combination of acid sites and metal active species.[9] The above properties of ASAs have enabled their widespread use in catalytic processes like hydrocarbon transformation, biomass conversion, hydrocracking, chemoselective hydrogenation, *etc.*[10,11]

For the sustainable chemical industry, many chemical processes that currently rely on corrosive and poisonous liquid acids (*e.g.*, HF and HCl) must be replaced with clean and safe

[a] *Laboratory for Catalysis Engineering, School of Chemical and Biomolecular Engineering, Sydney Nano Institute, the University of Sydney, NSW 2006, Australia. E-mail: jun.huang@sydney.edu.au*
[b] *Institute for Frontier Materials, Deakin University, Geelong, VIC 3220, Australia*
[c] *Faculty of Production Engineering, University of Bremen, Badgasteiner Straße 1, 28359, Bremen, Germany. E-mail: spokhrel@iwt.uni-bremen.de, lmaedler@iwt.uni-bremen.de*
[d] *Leibniz Institute for Materials Engineering IWT, Badgasteiner Straße 3, 28359 Bremen, Germany*
[e] *Australian Synchrotron, ANSTO, 800 Blackburn Rd, Clayton, VIC 3168, Australia*
[f] *MAPEX Center for Materials and Processes, University of Bremen, 28359 Bremen, Germany*

solid acids. However, the flexible tuning of acidity in solid acids remains a challenge. Unlike the easily tuned acidity of liquid acids, which can range from weak to superacids for the target reaction steps, the acidity of solid acids is limited by their local structure and overall electronegativity. On ASA, the unsaturated tetra-coordinated aluminum (Al^{IV}) species are generally regarded as key sites to replace tetra-coordinated silicon in the silica network for generating catalytically active Brønsted acid sites (BASs, Si–O(H^+)–Al).[12] It requires the atomic dispersion of Al species in the silica network and a lower Al fraction to avoid the generation of the low-dispersed alumina phase. Thus, both the density and strength of acid sites on ASA were not good enough to be tuned in a wide range from weak to strong acidity, although many traditional synthesis methods, including co-gelation, co-precipitation, and grafting, have been applied to improve the Al^{IV} species in the silica framework. Recently, another active aluminum species, the penta-coordinated aluminum species (Al^V), has been synthesized on silica–alumina and found to contribute to the formation of Brønsted acidity.[13–15] The majority of Al^V species are located on the accessible surface on ASA rather than the limited area at the interface.[13,14,16,17] The Al^V species is located near the surface SiOH group to form BAS *via* SiOHAl^V. This Al^V based BAS can be co-existing with Al^{IV} based BAS, rather than replacing each other. Thus, the density of acid sites is obviously enhanced.[13,14,17,18] In addition, free Al^V species nearby BAS can interact with the O atom in BAS to further enhance BAS acidity or form the zeolite type of the bridging OH group.[13,14,17,19] These strong acid sites on ASA can provide much lower activation energy in hydrocarbon activation *via* H/D exchange, compared to the most popular strong solid acid H-ZSM-5 zeolite.[20] It indicates the promising future of Al^V species based catalysts in chemical reactions, while the controlled synthesis of Al^V species remains challenging due to their metastable nature, as they tend to transform into the more stable Al^{IV} or Al^{VI} coordinations. Among the various approaches for synthesizing Al^V-enriched amorphous silica–alumina (ASA), flame spray pyrolysis (FSP) emerges as a highly promising technique, enabling the rapid and scalable production of ASA catalysts within microseconds.[21] The oxygen flow not only provides oxygen for flame but also provides O atoms for Si and Al oxides. In this research, we will tune the oxygen flow to adjust O atom coordination with Al species and then the local structure will be tuned for further tuning the surface acidity. These observations are consistent with recent reports showing that cooperative interactions between adjacent aluminum centers can significantly modulate both Brønsted acid strength and catalytic behavior in silica–alumina systems.[22]

Advanced characterization techniques are required to monitor and investigate the proposed synthesis–structure–function correlations. For ASA characterization in this research, solid state NMR is a powerful spectroscopic technology. 2D ^{27}Al multiple quantum (MQ) magic-angle spinning (MAS) NMR is the most powerful method to distinguish the various Al species in ASA.[23] Two-dimensional ^{27}Al through-space double-quantum to single-quantum (DQ-SQ) homonuclear correlation MAS NMR will describe the interaction between nearby Al species.[24,25] ^{1}H-^{27}Al 2D heteronuclear correlation (HETCOR) NMR is used to detect the interaction and bridging between Al species with surface SiOH for the formation of BAS.[26] ^{29}Si MAS NMR will monitor the distribution of Al species into the silica network, which can be double confirmed by near-edge X-ray absorption fine structure (NEXAFS).[27,28] The acidity of ASAs will be evaluated through ^{31}P MAS NMR investigation, following the adsorption of trimethylphosphine oxide (TMPO) as a probe molecule into dehydrated ASA samples.[29] The catalytic evaluation of ASA's acidity will be performed through the benzylation of various arenes, thus to complete the synthesis–structure–function correlation.

2. Experimental

2.1. Preparation of ASAs

ASA catalysts were synthesized using a gas phase flame aerosol technique. For the synthesis of amorphous aluminium–silica catalysts (ASA/50), 50 mL of aluminium-tri-*sec*-butoxide (97%, Sigma-Aldrich) and 50 mL of TEOS ($\geq$99%, Sigma-Aldrich) dissolved in xylene (99% purity, VWR) were mixed together to obtain a total concentration of 0.5 M. Similarly, for the synthesis of aluminium–silica catalysts (ASA/70), 70 mL of aluminium-tri-*sec*-butoxide and 30 mL of TEOS dissolved in xylene were mixed together (a total concentration of 0.5 M). In this study, catalysts are denoted as ASA/x_y, where $x = n\mathrm{Al}/(n\mathrm{Al} + n\mathrm{Si}) \times 100$ represents the mol% of the Al precursor in the Al–Si precursor mixture. The second number y refers to the dispersed O_2 flow rate (2.5, 5, or 7 L min^{-1}) used during flame spray pyrolysis. The precursor–solvent combination was fed into a two-fluid nozzle to form a spray flame combustion with constant premixed gas flows of 1.5 and 3.2 L min of CH_4 and O_2, respectively.[30,31] During the flame synthesis of ASA catalysts, the precursor–solvent flow was kept constant at 5 mL min^{-1}, while the dispersed O_2 flow was largely varied from 2.5 to 7 L min^{-1} with a constant pressure drop of 1.5 bar at the nozzle. The particles were collected on a glass fiber filter with 257 mm in diameter (Pall Laboratory A/F Glass) placed at a distance of 60 cm above the nozzle.[32]

2.2. Characterization

2.2.1. XRD and physical adsorption. Powder X-ray diffraction (XRD) measurements were performed using a PANalytical XPert Pro diffractometer operating with Co Kα radiation (λ = 0.1789 nm) in the Bragg–Brentano configuration. Nitrogen adsorption–desorption isotherms were recorded using an Autosorb iQ3 automated sorption system, and the specific surface areas of the samples were calculated using the Brunauer–Emmett–Teller (BET) approach.

2.2.2. Solid-state NMR spectroscopy. Magic angle spinning (MAS) NMR experiments were conducted using a Bruker Avance III 500WB spectrometer. Before measurement, the samples were subjected to dehydration by heating at 300 °C under vacuum conditions (below 10^{-2} mbar) overnight. To avoid contact with atmospheric moisture, the treated samples were

then transferred and sealed into MAS rotors inside a nitrogen-purged glovebox. Resonance frequencies of 500.1 MHz (^{1}H), 130.3 MHz (^{27}Al), 99.4 MHz (^{29}Si), and 202.5 MHz (^{31}P) were used. The spinning rate was 12 kHz for ^{1}H, ^{27}Al, ^{29}Si and ^{31}P using 4 mm MAS rotors. Spectra were acquired using single-pulse excitation with repetition times of 20 s (^{1}H, ^{29}Si), 0.5 s (^{27}Al), and 5 s (^{31}P).

For the acidity tests, trimethylphosphine oxide (TMPO, 5 wt%) was introduced as a probe molecule into dehydrated samples. The mixtures were subsequently heated to 160 °C to remove physically adsorbed TMPO. After weighing, the samples were loaded into MAS rotors under an inert atmosphere inside a nitrogen-filled glovebox. All MAS NMR experiments were performed using a 4 mm rotor at a spinning frequency of 12 kHz.

Two-dimensional ^{27}Al MQMAS NMR spectra were acquired employing a z-filtered three-pulse sequence, utilizing pulse widths of 3.0, 1.25, and 12 μs, along with a 200 ms recycle delay.[33] The experimental settings from the MQMAS analysis were subsequently applied to reconstruct the corresponding one-dimensional ^{27}Al MAS NMR spectra through simulation.

$$\mathrm{SOQE}^2 = \frac{\delta_{\mathrm{iso}} - \delta_{\mathrm{F2}}}{k} \quad (1)$$

$$\delta_{\mathrm{iso}} = \frac{17}{27}\delta_{\mathrm{F1}} + \frac{10}{27}\delta_{\mathrm{F2}} \quad (2)$$

$$k = \frac{3}{10}\frac{4I(I+1)-3}{[4I(2I-1)\nu_0]^2} \times 10^6 \quad (3)$$

$$\mathrm{SOQE} = C_{\mathrm{QCC}}\sqrt{1+(\eta^2/3)} \quad (4)$$

The second-order quadrupolar effect (SOQE) parameter is calculated based on the central positions of the contours in the F1 and F2 dimensions, represented by δ_{F1} and δ_{F2}. In this context, δ_{iso} indicates the isotropic chemical shift associated with the aluminum coordination environment, ν_0 corresponds to the Larmor frequency of the quadrupolar ^{27}Al nucleus (130.3 MHz), and I signifies its nuclear spin value of 5/2. Using the determined SOQE along with the asymmetry parameter (η), the quadrupolar coupling constant (C_{QCC}) can be subsequently extracted.

Two-dimensional ^{27}Al DQ–SQ MAS NMR experiments were carried out using a central transition (CT)-selective pulse sequence, employing π/2 and π pulses of 8 and 16 μs duration, respectively, under a radiofrequency (rf) field of approximately 10 kHz[9]. The generation and reconversion of double-quantum coherences were achieved *via* a BR recoupling sequence with durations ranging from 800 to 1200 μs and a rf amplitude of 6.6 kHz. To enhance polarization of the CT by suppressing satellite transitions, a hyperbolic secant (HS) saturation pulse (4 ms, 16 kHz rf, 20 kHz sweep width, and 200 kHz offset) was applied prior to the excitation. Autocorrelation signals located at coordinates (2ν, ν) in the resulting spectra indicate homonuclear interactions between identical aluminum sites, whereas cross-peaks at (ν_a + ν_b, ν_a) and (ν_a + ν_b, ν_b) reflect spatial proximities between chemically distinct Al species. For the ASA/70 sample, 14 400 and 3200 transients were collected for the DQ and SQ dimensions, respectively, using a 0.2 s recycle delay, resulting in total acquisition times of 25.3 and 5.7 hours. Chemical shifts for ^{27}Al were externally referenced to a 1 M aqueous solution of $Al(NO_3)_3$. Subsequently,^{1}H DQ–SQ spectra were recorded to investigate short-range dipolar interactions between protons. A symmetry-based recoupling scheme was used to reintroduce ^{1}H–^{1}H dipolar couplings under MAS conditions. π/2 pulses were applied at a radiofrequency amplitude of 75 kHz, while recoupling pulses were set at 60 kHz. The durations for excitation and reconversion ranged between 250 and 300 μs. Depending on the signal-to-noise requirement, 32 to 128 transients were averaged per spectrum with recycle delays varying from 1 to 5 s. Proton chemical shifts were calibrated to TMS using adamantane as a secondary reference (1.83 ppm).

The spatial interactions between ^{1}H and ^{27}Al nuclei were investigated using a two-dimensional heteronuclear correlation (HETCOR) NMR experiment.[13] Samples were packed into 2.5 mm MAS rotors and spun at 25 kHz. Cross-polarization contact times of 0.5 ms and 1 ms were employed to probe dipolar couplings. For each domain increment, 2500 scans were averaged with a 1 s recycle delay. A total of 16 increments were recorded to construct the full two-dimensional HETCOR spectra.

2.2.3. XAS investigation. The Al K-edge and Si K-edge XANES spectra were collected at the Soft X-ray beamline of the Australian Synchrotron (Clayton, VIC), which covers a wide photon energy range from 90 to 2500 eV.[34] The beamline is equipped with a collimated-light plane grating monochromator (PGM) illuminated using an elliptically polarized undulator (EPU), enabling high photon resolution and flux across the soft X-ray region. For Al K-edge (∼1560 eV) and Si K-edge (∼1840 eV) analysis, the 1200 lines per mm blazed grating was selected to ensure high spectral resolution, achieving a resolving power exceeding 5000 in the 1000–2000 eV range.

All optical components—including three fixed-angle mirrors set at a 1° glancing incidence and coated with 30 nm of gold—were optimized to ensure stable reflectivity across the full working range. During measurements, the vertical exit slit width was maintained at 20 μm, yielding an estimated photon energy resolution of ∼0.07–0.08 eV based on prior calibration using the N_2 1s → π* transition and the Fermi edge of a gold foil. The X-ray beam was directed onto the sample using a series of five optical components, and spectral data were collected in either total electron yield (TEY) or fluorescence yield (FY) mode, selected based on the sample's electrical conductivity and the specific detection needs.

2.3. Catalyst performance test

The liquid-phase benzylation reaction between mesitylene and benzyl alcohol was carried out in a 25 mL three-neck round-bottom flask placed in a thermostatically controlled oil bath. The reaction mixture was preheated to 373 K and held at this temperature for 30 minutes to ensure thermal equilibration.

Following this, 4 mmol of benzyl alcohol was rapidly introduced into the flask, marking the start of the reaction time. Reaction samples were periodically collected and analyzed using a Shimadzu GC-2010 gas chromatograph equipped with a Rtx-5 capillary column.

3. Results and discussion

3.1. Physical characterization

In this research, a series of ASA catalysts were prepared using the flame spray pyrolysis (FSP) process, yielding thermally stable, dry, and high-purity ASA catalysts in a single step. XRD patterns confirmed the amorphous structure of all catalysts (Fig. S1). Nitrogen adsorption/desorption isotherms (Fig. S2) indicated typical characteristics of dispersed nonporous particles, with surface areas summarized in Table 1. As the oxygen flow rate increased, the BET surface areas of ASA/50 and ASA/70 catalysts increased from 98 to 242 $m^2\ g^{-1}$ and 84 to 198 $m^2\ g^{-1}$, respectively, with the average particle sizes decreased from 17.7 to 7.1 nm and 20.6 to 8.6 nm, due to higher oxygen flow promoting better dispersion of silicon/Al atoms and inhibiting coagulation.[16]

3.2. Local structure of catalysts by ssNMR spectroscopy and XAS investigation

To overcome the significant line broadening typically associated with quadrupolar ^{27}Al nuclei, two-dimensional multiple-quantum magic-angle spinning (MQMAS) NMR spectroscopy was employed to resolve and differentiate the locally distorted environments of aluminum species.[13,35] For the ASA/50 and ASA/70 catalysts, as shown in Fig. 1A–F, three distinct contours were identified in the spectrum, corresponding to four-coordinated (a: δ_{iso} = 56 ppm and b: δ_{iso} = 41 ppm), five-coordinated (a: δ_{iso} = 33 ppm and b: δ_{iso} = 18 ppm), and six-coordinated (δ_{iso} = 3–9 ppm) aluminum species. A comparison of quadrupole coupling constant (C_{QCC}) values revealed that Al^{IV}b and Al^{V}b exhibit significantly higher values than Al^{IV}a and Al^{V}a, indicating a more distorted local structure,[36] which may be caused by the nearby Al^{IV} and Al^{V} species interacting each other. Both Al^{IV} and Al^{V} species can be located adjacent to surface silanol (SiOH) groups, generating bridging or pseudo-bridging SiOHAl groups to form Brønsted acid sites (BASs).[13,37]

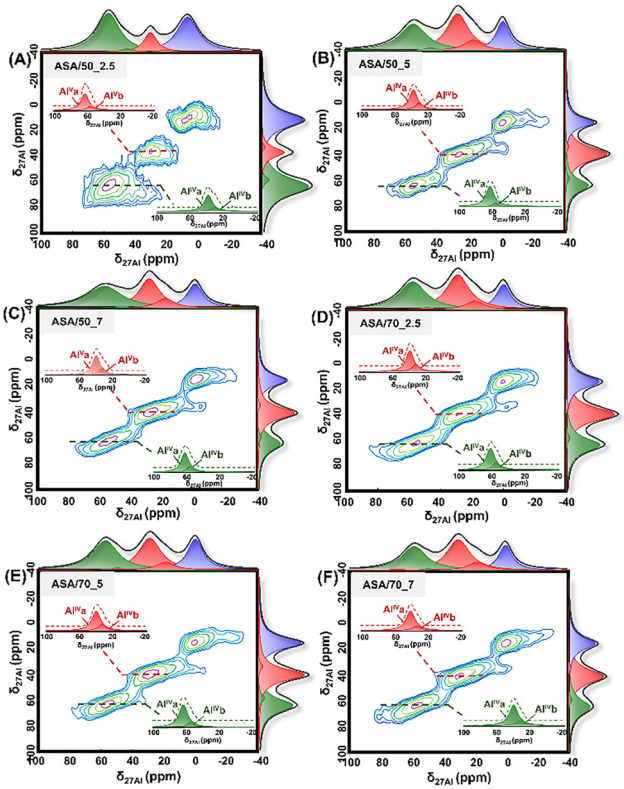

Fig. 1 2D ^{27}Al multiple quantum MAS NMR spectra of (A) ASA/50_2.5, (B) ASA/50_5, (C) ASA/50_7, (D) ASA/70_2.5, (E) ASA/70_5, and (F) ASA/70_7 catalysts.

Using the MQMAS spectral data and the extracted quadrupolar parameters summarized in Fig. 1 and Table S1, the one-dimensional ^{27}Al single-pulse MAS NMR spectra were simulated, as shown in Fig. 2. Al^{V} species is dominant in all samples at a fraction from 36.63% to 49.19% with Al^{IV} and Al^{VI} species from 42.63% to 48.23%, when the oxygen flow increases from 2.5 to 7 mL min^{-1}. Among these species on ASA/50_2.5, ASA/50_5, ASA/50_7, ASA/70_2.5, ASA/70_5, and ASA/70_7, both Al^{IV}a and Al^{V}a mole fractions decreased from 26.4 to 22.0% and 29.2 to 17.1%, respectively. However, the mole fraction of Al^{IV}b and Al^{V}b species increased from 10.3 to 24.2% and 13.5 to 30.2%, respectively. All Al^{IV} and Al^{V} species are incorporated into the silica network. However, the Al^{IV}b and Al^{V}b species exhibit a more highly distorted coordination environment and stronger interaction

Table 1 Summary of physical characterization, deconvolution of aluminum species ratios, and acid concentrations and fractions for the ASA/50 and ASA/70 catalysts

Catalysts	SSA[a] ($m^2\ g^{-1}$)	d_{BET}[a] (nm)	Al^{IV}a (%)	Al^{IV}b (%)	Al^{V}a (%)	Al^{V}b (%)	Al^{VI} (%)	BAS ($\times10^{-2}$ mmol g^{-1})	LAS ($\times10^{-2}$ mmol g^{-1})	B/L
ASA/50_2.5	97.9	17.7	26.35	10.28	29.16	13.47	20.64	4.0	2.5	1.60
ASA/50_5	177.8	9.6	25.60	17.31	23.75	14.32	18.94	4.6	2.5	1.84
ASA/50_7	242.0	7.1	21.70	17.49	21.14	21.53	18.14	5.1	3.0	1.71
ASA/70_2.5	83.9	20.6	25.67	17.58	21.86	23.28	11.62	7.2	3.8	1.92
ASA/70_5	140.6	12.2	26.31	23.13	18.99	24.23	7.34	7.8	4.1	1.90
ASA/70_7	198.0	8.6	22.03	24.16	17.08	30.15	6.57	8.5	4.1	2.07

[a] Specific surface area, d_{BET}: primary particle size obtained from BET.

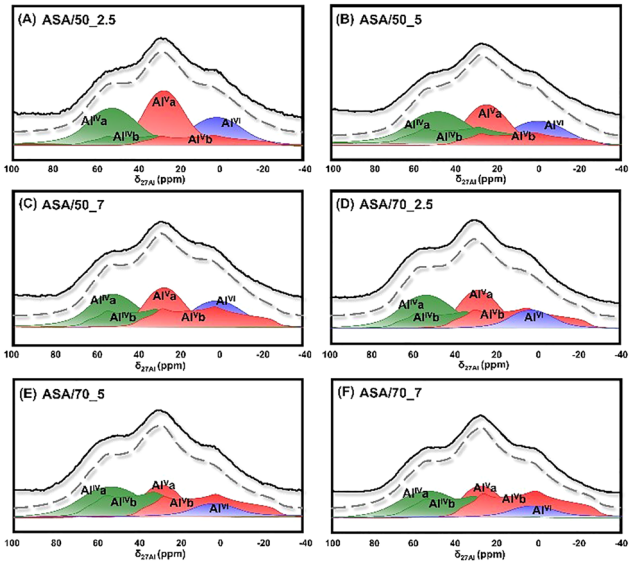

Fig. 2 ^{27}Al MAS NMR spectra of (A) ASA/50_2.5, (B) ASA/50_5, (C) ASA/50_7, (D) ASA/70_2.5, (E) ASA/70_5, and (F) ASA/70_7 dehydrated at 573 K under a vacuum for 12 h. Experiment (top, solid line), simulation line (top, dash line), and components (bottom, solid lines).

with the silica network, as indicated by ^{29}Si cross-polarization (CP) MAS NMR investigations of dehydrated ASA samples prepared by the increased oxygen flow. ^{29}Si CP MAS NMR only shows the local environment of surface Si species with OH groups; as shown in Fig. 3A and B, the peak slightly shifts to a lower field with an increasing oxygen flow rate both in the ASA/50 and ASA/70 catalysts. This indicates that more Al species incorporate into the surface silica network under the increased oxygen flow rate during FSP synthesis.[5,38] It correlates well with the above ^{27}Al MAS NMR study that more Al^{IV}b and Al^{V}b incorporate with nearby SiOH.

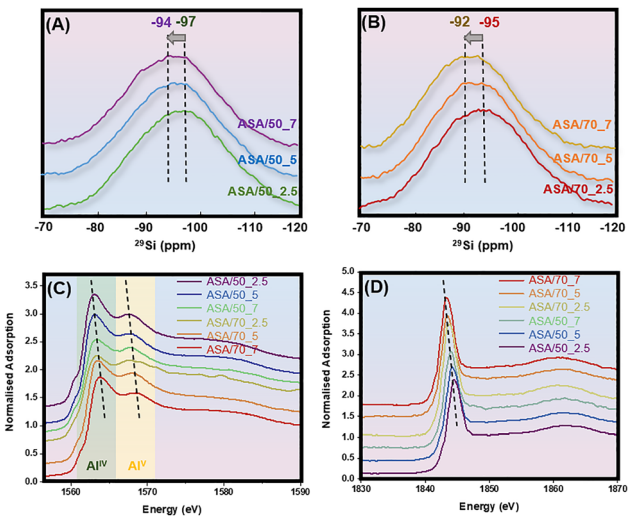

Fig. 3 ^{29}Si cross-polarization MAS NMR spectra of ASA/50 (A) and ASA/70 (B) with O_2 flow rates of 2.5, 5, and 7 L min^{-1}. Al K-edge (C) and Si K-edge (D) for all ASA catalysts.

Al and Si K-edge XANES investigation also confirmed that more Al species incorporate into the surface silica network with an increased oxygen flow rate during FSP synthesis. From XANES spectra, it is possible to predict the coordination environment of Al from the energy position of the K absorption edge; the exact energy of this 1s to 3p electron transition depends on the coordination number of the coordination sphere around the atom.[39] As shown in Fig. 3C, Al K-edge XAS spectra exhibit two dominant broad peaks at 1563–1564 eV (a) and 1568–1569 eV (b) assigned to Al^{IV} and Al^{V} species, respectively, and one broad peaks at around 1580 eV (c) may be caused by Al^{VI} species.[40–42] In general, the Al K-edge shifts to higher energy with increase in the numbers of aluminium coordination.[42] With the oxygen flow rate increasing for the ASA synthesis, both peaks for Al^{IV} and Al^{V} species shift to high energy, indicating the strongly distorted Al environments of both species.[43] This observation corelates very well with the ^{27}Al MAS NMR spectra.

Fig. 3D shows the Si K-edge XANES spectra of the prepared ASA catalysts. The strong dominant peak observed between 1843 and 1844 eV corresponds to the electronic transition of Si 1s to 3p.[44] The broader peaks appearing between 1857 and 1865 eV are attributed to higher-energy shape resonances.[45] With increasing oxygen flow and more Al fraction during synthesis, the Si K-edge shifts to lower energies from 1844 eV in ASA/50_2.5 to 1843 eV in ASA/70_7. It is reported that the substitution of Al for Si lowers the effective charge on the silicon atoms because the Al–O bond is weaker than the Si–O bond, facilitating electron density redistribution and causing the Si K-edge shift to lower energy.[44] This observation also correlates very well with ^{29}Si CP MAS NMR spectra that aluminum species become incorporated into silica frameworks, modifying local silicon environments.

3.3. ssNMR investigation of BAS formation and the surface acidity

^{1}H MAS NMR spectra of ASA samples in Fig. S3 are dominated by a strong signal at δ_{1H} = 2.3 ppm, which is caused by the surface SiOH groups on ASAs.[16] The above observed incorporation of Al^{IV} and Al^{V} species into silica frameworks can generate the surface Si–OH···Al$^{IV/V}$ groups, which is BAS on ASA.[46] This kind of incorporation will induce a dipolar coupling between ^{27}Al and ^{1}H nuclei, which can be effectively probed through two-dimensional ^{1}H–^{27}Al CP/MAS HETCOR NMR investigation. As shown in Fig. 4a, the correlation at δ_{27Al} = 47 ppm of Al^{IV} species and δ_{27Al} = 21 ppm of Al^{V} species with δ_{1H} = 2.3 ppm in the ^{1}H–^{27}Al CP/MAS HETCOR NMR spectrum of dehydrated ASA/70_7 indicates the formation of Si–OH···Al$^{IV/V}$ groups, which is the typical BAS-Al^{IV} or BAS-Al^{V} structure for acid ASA.[18] They are not bridging SiOHAl groups like zeolites, as δ_{1H} is around 3.6–5.2 ppm for bridging OH groups or disturbed bridging OH groups. Si–OH···Al$^{IV/V}$ are pseudo-bridging groups between Al species and nearby silanols.[37,47] The electron-withdrawing nature of Al species to nearby surface SiOH groups would generate the acidic proton on Si–OH···Al$^{IV/V}$ as Brønsted acid sites.[18,48] A very weak correlation at δ_{27Al} = 0 ppm of Al^{VI}

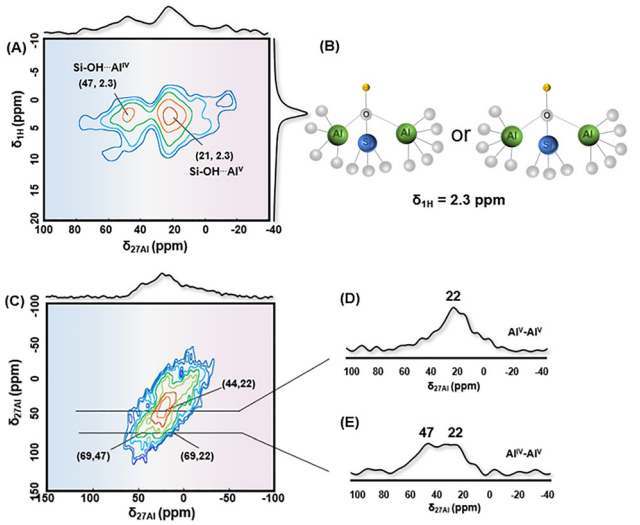

Fig. 4 (A) $^{1}H-^{27}Al$ HETCOR MAS NMR spectra of ASA/70_7 and (B) proposed models for BASs on ASAs. (C) 2D ^{27}Al DQ–SQ NMR spectrum of the representative ASA/70_7 catalyst. (D and E) Rows extracted from the two-dimensional spectrum represent distinct autocorrelation and cross-peak features. Each row is presented on an identical intensity scale.

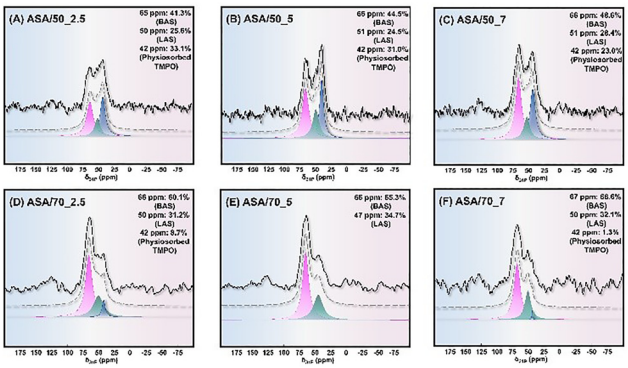

Fig. 5 ^{31}P MAS NMR spectra of TMPO adsorbed on (A) ASA/50_2.5, (B) ASA/50_5, (C) ASA/50_7, (D) ASA/70_2.5, (E) ASA/70_5, and (F) ASA/70_7 samples. Experiment (top, solid line), simulation line (top, dash line), and components (bottom, solid lines).

species and δ_{1H} = 1.1 ppm of AlOH groups is assigned to non-acidic terminal $Al^{VI}OH$ groups, which indicates that Al^{VI} species do not incorporate with the silica network to form the acid sites. Fig. 4A displays a dominant contour centered at (δ_{1H} = 2.3 ppm and δ_{27Al} = 21 ppm), indicating that the mainly Brønsted acid sites on ASA/70_7 are associated with Si–OH···Al^{V} groups at the surface. The density of BASs increases with the increased fraction of Al^{V}b species on ASAs. As shown in Table 1, the mole fractions of Al^{V}b of 23.3%, 24.2%, and 30.2% for ASA/70_2.5, ASA/70_5, and ASA/70_7, respectively, correlate with the increase in surface BAS concentrations of 7.2 × 10^{-2} mmol g^{-1}, 7.8 × 10^{-2} mmol g^{-1}, and 8.5 × 10^{-2} mmol g^{-1} for these ASA samples.

Since the mole fraction of Al species is higher than that of Si species, there should be existing two Al species nearby one Si species. Spatial proximities among ^{27}Al nuclei were examined using two-dimensional through-space ^{27}Al DQ–SQ homonuclear correlation MAS NMR, as illustrated in Fig. 4C. The most prominent feature is a diagonal peak located at (44, 22) ppm, corresponding to the Al^{V} site in the ASA/70_7 sample (Fig. 4C and its associated projection in Fig. 4D). This strong autocorrelation signal signifies the presence of adjacent Al^{V} sites, suggesting their uniform distribution and high surface concentration. Additionally, two intense off-diagonal cross-peaks at (69, 47) and (69, 22) ppm confirm the close spatial relationship between Al^{V} species (δ = 22 ppm) and Al^{IV} centers (δ = 47 ppm), as supported by Fig. 4C and the corresponding slice in Fig. 4E. Furthermore, the two-dimensional ^{1}H DQ–SQ spectrum (Fig. S4) reveals a dominant correlation at (3.4, 1.7) ppm and a weaker one at (4.2, 2.1) ppm, indicating the presence of spatially adjacent silanol groups across the surface.

To elucidate the relationship between structure and acidity in ASA materials, ^{31}P MAS NMR spectroscopy was performed using trimethylphosphine oxide (TMPO) as a molecular probe.[49–51] This technique enables the differentiation of acid sites with varying strengths by analyzing the chemical shifts of adsorbed or reacted TMPO species. As depicted in Fig. 5A–F, shifts in the ^{31}P resonance positions provide insight into the type and strength of surface acid sites.[52–54] Typically, downfield shifts in the ^{31}P signal are indicative of stronger Brønsted acidity, as these sites withdraw more electron density from the phosphorus nucleus, resulting in reduced shielding.[55,56] Based on peak deconvolution (Fig. 5), the dominant signal in the 65–67 ppm range corresponds to TMPO coordinated with Brønsted acid sites (BASs). The peaks located between 47 and 51 ppm in Fig. 5A–F are assigned to TMPO interacting with Lewis acid sites (LAS), which are typically associated with trigonal (3-coordinate) or distorted/penta-coordinate aluminum species, rather than fully coordinated octahedral Al.[55,57,58] A separate resonance at approximately 42 ppm arises from physisorbed TMPO molecules.[48,59] Quantitative analysis of the signal intensities allows for the estimation of the relative populations of BAS and LAS, as shown in Fig. 5, with the calculated molar fractions summarized in Table 1. Both Brønsted and Lewis acid site densities increase progressively from ASA/50 to ASA/70 as the oxygen flow rate during synthesis is elevated. This trend aligns with the growing presence of Si–OH–Al^{IV}b or Al^{V}b, suggesting that these aluminum environments are closely associated with surface silanol groups and function as catalytically active acid sites in ASA catalysts.

In most ASAs synthesized using traditional methods, only moderate Brønsted acid site (BAS) strength (δ_{31P} = 61–62 ppm, as probed by TMPO) has been detected.[13] This moderate acidity is thought to result from a single aluminum center interacting with a neighboring silanol group, thereby reducing the electron density of the oxygen atom and forming an acidic SiOH site. This configuration is comparable to the pseudobridging silanol (PBS) model proposed in previous theoretical studies, where a SiOH group electrostatically interacts with an Al center (Al^{IV} or Al^{V}) without forming a covalent bond, unlike the bridging OH groups typically found in zeolites.[37,60]

In contrast to conventional ASAs, those synthesized *via* flame spray pyrolysis (FSP), such as FSP ASA/50 and ASA/70, exhibit the

Table 2 Resonance positions (δ_{31P}) Of TMPO molecules absorbed at the Brønsted acid sites and the BAS structure of FSP ASAs, traditional synthesized ASAs and zeolite

Acids	δ_{31P} (ppm)	BAS structure	Ref.
HY	63–65		62 and 63
H-MCM-22	66		64
H-ZSM-5	64–73		55, 65 and 66
ASAs	61–62	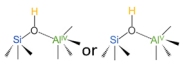	13
FSP ASAs	65–67	PBS (one Al center with SiOH) —	This work

unique structural feature wherein two aluminum species, either both Al^{V} or a combination of Al^{V} and Al^{IV}, are positioned in close proximity to a single surface SiOH group. A study by Valla *et al.*, which integrated dynamic nuclear polarization (DNP) NMR with first-principles calculations, proposed structural motifs for ASA materials that support this arrangement.[61] Their models, developed for ASAs prepared by chemical liquid deposition of SiO_2 on Al_2O_3, suggest that multiple Al centers can cluster near a silanol group. This hypothesis is further corroborated by radial distribution function (RDF) analyses, which reveal a tendency for Al species to aggregate, particularly in high-Al-content ASAs such as ASA/50.[14] Consequently, it is reasonable to expect the coexistence of multiple Al centers near a single SiOH moiety in both ASA/50 and ASA/70.

Building on these insights, we propose a structural model for Brønsted acid site (BAS) formation in ASA/50 and ASA/70 (Fig. 4b). In this model, the presence of a second, unsaturated neighboring aluminum atom plays a dual role: it acts as an auxiliary Lewis acid site, stabilizing the deprotonated silanolate intermediate, and it enhances electron withdrawal from the bridging oxygen of the SiOH group.[47,60] This dual-Al environment significantly amplifies the proton-donating capability of the site, resulting in an observed BAS strength as high as δ_{31P} = 67 ppm. This value exceeds the Brønsted acid strength reported for zeolite H–Y (δ_{31P} = 63–65 ppm)[62,63] and aligns closely with highly active systems like H-MCM-22 (δ_{31P} = 66 ppm)[64] and H-ZSM-5 (δ_{31P} = 64–73 ppm),[55,65,66] as summarized in Table 2.

This proposed model mirrors mechanisms observed in zeolitic frameworks, where extra-framework Al species enhance Brønsted acidity *via* an electrostatic effect. Accordingly, the cooperative interaction between two adjacent aluminum centers, whether Al^{V}–Al^{V} or Al^{IV}–Al^{V}, is anticipated to substantially elevate the acid strength of BAS in ASA materials, contributing to their catalytic performance (Fig. 5).

4. Catalyst performance test

To evaluate the catalytic performance of ASA materials in terms of both activity and selectivity, benzylation reactions of arenes including benzene, toluene, *p*-xylene, and mesitylene with

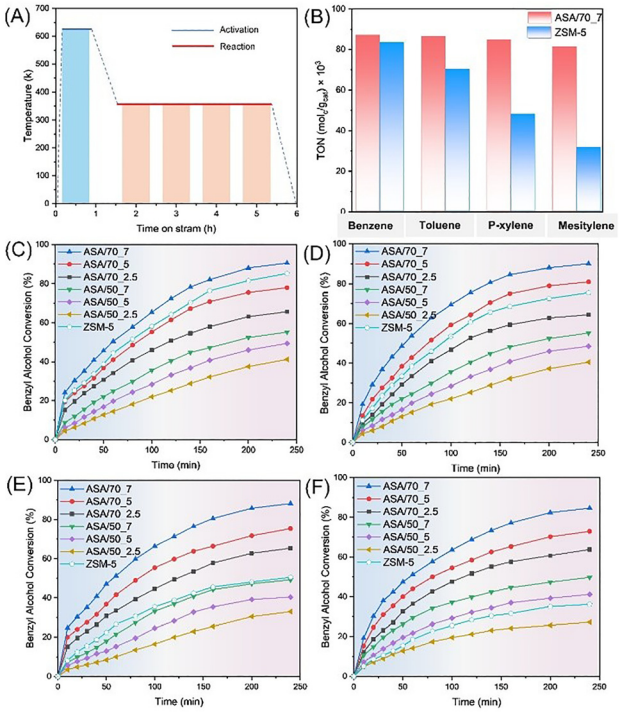

Fig. 6 (A) Temperature program of the reaction at 353 K after activation at 623 K for 1 h. (B) Reaction performance of the ASA/70_7 catalyst compared to that of the ZSM-5 catalyst. Benzyl alcohol conversion in the benzylation of different arenes over various ASAs and ZSM-5 catalysts: (C) benzene, (D) toluene, (E) *p*-xylene, and (F) mesitylene. Conditions: 25 mg catalysts, 3.5 mL arenes, 0.25 mL benzyl alcohol, and a reaction temperature of 353 K.

benzyl alcohol were conducted at 353 K for 4 hours (Fig. 6A). As presented in Fig. 6, the conversion of benzyl alcohol over different ASA catalysts varied with time, following the trend ASA/70_7 > ASA/70_5 > ASA/70_2.5 > ASA/50_7 > ASA/50_5 > ASA/50_2.5, which closely mirrors the Brønsted acid site concentrations summarized in Table 1. This observation supports previous findings that higher Brønsted acid densities promote more efficient activation of benzyl alcohol.[67] In this context, increasing the aluminum content and oxygen flow rate during FSP synthesis led to a greater concentration of Brønsted acid sites, thereby enhancing overall catalytic activity. In terms of selectivity, Table 3 shows that the production of monobenzylated compounds followed the sequence ASA/50_2.5 < ASA/50_7 < ASA/50_5 < ASA/70_5 < ASA/70_2.5 < ASA/70_7, which is consistent with the increasing Brønsted-to-Lewis acid site ratios reported in Table 1. These findings highlight the critical role of acid site balance,[68] where Brønsted sites promote electrophilic substitution while Lewis sites suppress the self-condensation of benzyl alcohol.[69] This synergistic interaction between acid site types ultimately governs the product distribution, as illustrated in Scheme 1.[70] The major reaction products include dibenzyl ether (DBE), diphenylmethane (DPM), benzyl-4-methylbenzene (4-BMB), 2-benzyl-1,4-dimethylbenzene (BDB), and 2-benzyl-1,3,5-trimethylbenzene (BTB), which originate from two competing pathways. DBE is formed through the self-condensation of benzyl

Table 3 Conversion and selectivity in the benzylation of benzyl alcohol with arenes over ASAs[a]

		Conversion% (selectivity%)					
Arenes	Products	ASA/50_2.5	ASA/50_5	ASA/50_7	ASA/70_2.5	ASA/70_5	ASA/70_7
Benzene	DPM	41.2 (68.8)	50.4 (72.1)	55.2 (70.6)	65.7 (85.6)	78.1 (78.2)	90.5 (86.3)
Toluene	4-BMB	40.5 (65.7)	48.5 (70.4)	55.2 (66.1)	64.3 (79.0)	81.8 (73.6)	90.0 (79.3)
p-Xylene	BDB	33.0 (73.8)	40.5 (77.1)	49.2 (76.9)	65.4 (89.1)	75.4 (86.4)	88.2 (90.2)
Mesitylene	BTB	27.2 (76.4)	41.1 (80.2)	49.8 (80.0)	63.8 (92.5)	73.0 (88.3)	84.7 (94.1)

[a] Conditions: 25 mg catalysts, 3.5 mL arenes, 0.25 mL benzyl alcohol, reacted at 353 K for 4 h. DPM, BMB, BDB and BTB are for diphenylmethane, benzyl-methylbenzene, 2-benzyl-1,4-dimethylbenzene and 2-benzyl-1,3,5-trimethylbenzene.

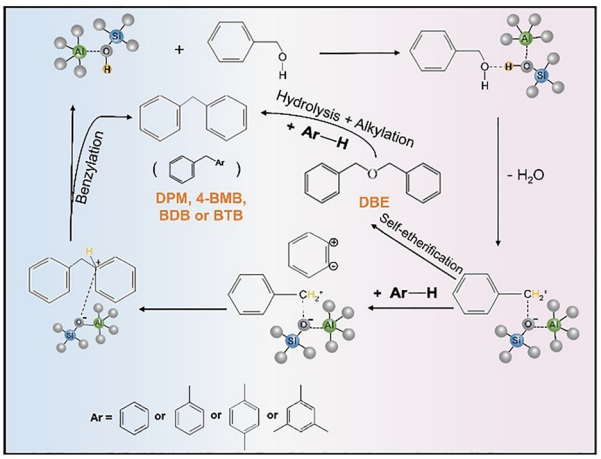

Scheme 1 Proposed reaction pathways for benzylation over ASAs.

alcohol, while the monobenzylated products result from direct electrophilic benzylation of the aromatic ring. In comparison to ZSM-5 catalysts (Fig. 6B–F), where the catalytic efficiency decreases with increasing molecular size due to diffusion limitations in microporous channels.[71] ASA catalysts alleviate these issues through their mesoporous structure, thus enabling improved performance across a broader range of substrates.

To assess the long-term usability of the FSP-derived ASAs, recyclability tests were performed using the most active catalyst, ASA/70_7, in the benzylation of arenes (Fig. S5). After each reaction, the catalyst was recovered by centrifugation, washed with ethanol, dried at 373 K, and reused without further treatment. The conversion of benzyl alcohol still showed very stable performance, while the selectivity toward aimed products remained above 80% throughout all cycles. These results confirm the high structural stability of the surface Al^V–SiOH Brønsted acid sites generated *via* FSP and demonstrate that the catalysts possess excellent recyclability suitable for practical applications.

Conclusions

In this work, we have demonstrated that tailoring the coordination environment of aluminum species on amorphous silica–alumina (ASA) *via* flame spray pyrolysis (FSP) can effectively enhance surface acidity and catalytic performance in arene benzylation. By tuning the oxygen flow during synthesis, we promoted the formation of penta-coordinated aluminum (Al^V) species, particularly the surface distorted Al^Vb type, which were found in close proximity to SiOH groups and acted as key contributors to strong Brønsted acid sites (BASs). Advanced solid-state NMR and XAS analyses confirmed the incorporation of Al^V into the silica network and its role in forming pseudo-bridging acidic sites. The resulting ASA catalysts exhibited improved acid strength, as shown by ^{31}P MAS NMR, and superior activity and selectivity in benzylation reactions. This study establishes a clear synthesis–structure–acidity–function relationship, demonstrating that flame-made ASAs achieve zeolite-like acidity through cooperative interactions between Al^V species and neighboring Al sites near silanols, rather than through conventional bridging hydroxyls. The combination of advanced NMR techniques provides compelling evidence for this unique dual-Al-site mechanism of acidity enhancement.

Author contributions

J. Huang. designed the study. Haipeng Li. prepared the catalysts. X. Liu., L. O'Dell. and W. Yang performed the NMR experiments. X. Liu performed the structural assignment. Q. Gu performed the NEXAFS experiments. X. Liu contributed to the catalytic reaction test. J. Huang. supervised scientific work. X. Liu contributed to writing the paper, and X. Liu., S. Pokhrel, L. Mädler and J. Huang revised it.

Conflicts of interest

The authors declare that they have no known competing financial interests or personal relationships that could have appeared to influence the work reported in this paper.

Data availability

The data supporting this article have been included as part of the supplementary information (SI). The supplementary information includes additional structural and spectroscopic characterization data, including XRD patterns, N_2 adsorption–desorption isotherms, detailed ^{27}Al NMR fitting parameters, ^{1}H MAS and DQ–SQ NMR spectra, and catalyst regeneration performance data. See DOI: https://doi.org/10.1039/d5ey00312a.

Acknowledgements

This work is financially supported by the Australian Research Council Discovery Project (DP220102851) and the ARC Future Fellowships (FT220100601). Authors acknowledge facilities of Sydney Analytical, a core research facility at the University of Sydney, and NMR facility of Deakin University. Part of the experiment was conducted at SXR beamline, Australian Synchrotron, ANSTO.

References

1 D. Yun, Y. S. Yun, T. Y. Kim, H. Park, J. M. Lee, J. W. Han and J. Yi, *J. Catal.*, 2016, **341**, 33–43.
2 G. Busca, *Chem. Rev.*, 2007, **107**, 5366–5410.
3 J. Bao, Q.-h Yang, S.-q Zeng, X.-y Sang, W.-m Zhai and H. Nie, *Microporous Mesoporous Mater.*, 2022, **337**, 111897.
4 J. Ge, J. Sun, P. Zhang, Z. Xie, Z. Wu and B. Liu, *Catal. Sci. Technol.*, 2022, **12**, 3695–3705.
5 K. D. Kim, S. Pokhrel, Z. Wang, H. Ling, C. Zhou, Z. Liu, M. Hunger, L. Mädler and J. Huang, *ACS Catal.*, 2016, **6**, 2372–2381.
6 J. Horlyck, S. Pokhrel, E. Lovell, N. M. Bedford, L. Mädler, R. Amal and J. Scott, *Catal. Sci. Technol.*, 2019, **9**, 4970–4980.
7 N. Fang, K. Huo, Y. Jin, D. Liu, H. Lin, H. Wu, X. Liu, Y. Liu and M. He, *ACS Catal.*, 2024, **14**, 4786–4790.
8 G. Crépeau, V. Montouillout, A. Vimont, L. Mariey, T. Cseri and F. Maugé, *J. Phys. Chem. B*, 2006, **110**, 15172–15185.
9 Z. Wang, Y. Jiang, F. Jin, C. Stampfl, M. Hunger, A. Baiker and J. Huang, *J. Catal.*, 2019, **372**, 1–7.
10 A. Ishihara, *Catal. Surv. Asia*, 2012, **16**, 36–47.
11 T. Li, L. Zhang, Z. Tao, C. Hu, C. Zhao, F. Yi, X. Gao, X. Wen, Y. Yang and Y. Li, *Fuel*, 2020, **279**, 118487.
12 M. Trombetta, G. Busca, S. Rossini, V. Piccoli, U. Cornaro, A. Guercio, R. Catani and R. J. Willey, *J. Catal.*, 1998, **179**, 581–596.
13 W. Yang, X. Liu, L. A. O'Dell, L. Wang, Y. Jiang and J. Huang, *J. Phys. Chem. C*, 2023, **127**, 23212–23222.
14 Z. Wang, T. Li, Y. Jiang, O. Lafon, Z. Liu, J. Trébosc, A. Baiker, J.-P. Amoureux and J. Huang, *Nat. Commun.*, 2020, **11**, 225.
15 W. Liu, H. Zhao, X. Wu, G. Dury, W. Hu and W. Liu, *J. Energy Chem.*, 2025, **111**, 178–189.
16 Z. Wang, Y. Jiang, X. Yi, C. Zhou, A. Rawal, J. Hook, Z. Liu, F. Deng, A. Zheng and M. Hunger, *Sci. Bull.*, 2019, **64**, 516–523.
17 W. Yang, X. Liu, L. A. O'Dell, X. Liu, L. Wang, W. Zhang, B. Shan, Y. Jiang, R. Chen and J. Huang, *JACS Au*, 2023, **3**, 2586–2596.
18 Z. Wang, Y. Jiang, O. Lafon, J. Trébosc, K. Duk Kim, C. Stampfl, A. Baiker, J.-P. Amoureux and J. Huang, *Nat. Commun.*, 2016, **7**, 13820.
19 Z. Wang, R. Buechel, Y. Jiang, L. Wang, H. Xu, P. Castignolles, M. Gaborieau, O. Lafon, J.-P. Amoureux and M. Hunger, *JACS Au*, 2021, **1**, 262–271.
20 Z. Wang, Y. Jiang, A. Baiker, M. Hunger and J. Huang, *J. Phys. Chem. Lett.*, 2022, **13**, 486–491.
21 H. K. Kammler, L. Mädler and S. E. Pratsinis, *Chem. Eng. Technol.*, 2001, **24**, 583–596.
22 L. Chen, W. Wang, T. Lu, X. Luo, X. Xie, K. Huang, S. Qin, T. Su, Z. Qin and H. Ji, *Acta Phys.-Chim. Sin.*, 2025, **41**, 100054.
23 J. Ashenhurst, S. Wang and G. Wu, *J. Am. Chem. Soc.*, 2000, **122**, 3528–3529.
24 M. Zheng, Q. Wang, Y. Chu, X. Tan, W. Huang, Y. Xi, Y. Wang, G. Qi, J. Xu and S. B. Hong, *J. Am. Chem. Soc.*, 2024, **146**, 29417–29428.
25 F. A. Perras, Z. Wang, T. Kobayashi, A. Baiker, J. Huang and M. Pruski, *Phys. Chem. Chem. Phys.*, 2019, **21**, 19529–19537.
26 R. Verma, C. Singhvi, A. Venkatesh and V. Polshettiwar, *Nat. Commun.*, 2024, **15**, 6899.
27 C. J. Heard, L. Grajciar, C. M. Rice, S. M. Pugh, P. Nachtigall, S. E. Ashbrook and R. E. Morris, *Nat. Commun.*, 2019, **10**, 4690.
28 J. A. van Bokhoven, A. M. Van der Eerden and D. C. Koningsberger, *J. Am. Chem. Soc.*, 2003, **125**, 7435–7442.
29 A. Zheng, H. Zhang, X. Lu, S.-B. Liu and F. Deng, *J. Phys. Chem. B*, 2008, **112**, 4496–4505.
30 M. Minnermann, S. Pokhrel, K. Thiel, R. Henkel, J. Birkenstock, T. Laurus, A. Zargham, J.-I. Flege, V. Zielasek and E. Piskorska-Hommel, *J. Phys. Chem. C*, 2011, **115**, 1302–1310.
31 M. Gäßler, J. Stahl, M. Schowalter, S. Pokhrel, A. Rosenauer, L. Mädler and R. Güttel, *ChemCatChem*, 2022, **14**, e202200286.
32 H. Li, C. Erinmwingbovo, J. Birkenstock, M. Schowalter, A. Rosenauer, F. La Mantia, L. Mädler and S. Pokhrel, *ACS Appl. Energy Mater.*, 2021, **4**, 4428–4443.
33 C. A. Fyfe, J. L. Bretherton and L. Y. Lam, *J. Am. Chem. Soc.*, 2001, **123**, 5285–5291.
34 B. C. C. Cowie, A. Tadich and L. Thomsen, *AIP Conf. Proc.*, 2010, **1234**, 307–310.
35 Z. Wang, K. Chen, Y. Jiang, J. Trébosc, W. Yang, J.-P. Amoureux, I. Hung, Z. Gan, A. Baiker and O. Lafon, *J. Phys. Chem. Lett.*, 2021, **12**, 11563–11572.
36 T.-H. Chen, K. Houthoofd and P. J. Grobet, *Microporous Mesoporous Mater.*, 2005, **86**, 31–37.
37 C. Chizallet and P. Raybaud, *Angew. Chem.*, 2009, **121**, 2935–2937.
38 B. Sun, S. Pokhrel, D. R. Dunphy, H. Zhang, Z. Ji, X. Wang, M. Wang, Y.-P. Liao, C. H. Chang and J. Dong, *ACS Nano*, 2015, **9**, 9357–9372.
39 A. Omegna, R. Prins and J. A. Van Bokhoven, *J. Phys. Chem. B*, 2005, **109**, 9280–9283.
40 J. Wong, Z. Rek, M. Rowen, T. Tanaka, F. Schäfers, B. Müller, G. George, I. Pickering, G. Via and B. DeVries, *Phys. B*, 1995, **208**, 220–222.
41 M. Fröba, J. Wong, M. Rowen, G. Brown Jr, T. Tanaka and Z. Rek, *Phys. B*, 1995, **208**, 555–556.
42 D. Li, G. Bancroft, M. Fleet, X. Feng and Y. Pan, *Am. Mineral.*, 1995, **80**, 432–440.

43 J. L. Fulton, N. Govind, T. Huthwelker, E. J. Bylaska, A. Vjunov, S. Pin and T. D. Smurthwaite, *J. Phys. Chem. B*, 2015, **119**(26), 8380–8388.
44 D. Li, G. Bancroft, M. Fleet and X. Feng, *Phys. Chem. Miner.*, 1995, **22**, 115–122.
45 J. L. Dehmer, *J. Chem. Phys.*, 1972, **56**, 4496–4504.
46 Z. Wang, S. Pokhrel, M. Chen, M. Hunger, L. Mädler and J. Huang, *J. Catal.*, 2013, **302**, 10–19.
47 C. Chizallet and P. Raybaud, *ChemPhysChem*, 2010, **11**, 105–108.
48 Z. Wang, Y. Jiang, A. Baiker and J. Huang, *ACS Catal.*, 2013, **3**, 1573–1577.
49 C. Wang, W. Dai, G. Wu, N. Guan and L. Li, *Magn. Reson. Lett.*, 2022, **2**, 28–37.
50 W. Yang, Z. Wang, J. Huang and Y. Jiang, *J. Phys. Chem. C*, 2021, **125**, 10179–10197.
51 Z. Wang, Y. Jiang, C. Stampfl, A. Baiker, M. Hunger and J. Huang, *ChemCatChem*, 2020, **12**, 287–293.
52 L. Lakiss, A. Vicente, J. P. Gilson, V. Valtchev, S. Mintova, A. Vimont, R. Bedard, S. Abdo and J. Bricker, *ChemPhysChem*, 2020, **21**, 1873–1881.
53 C. Bornes, M. Sardo, Z. Lin, J. Amelse, A. Fernandes, M. F. Ribeiro, C. Geraldes, J. Rocha and L. Mafra, *Chem. Commun.*, 2019, **55**, 12635–12638.
54 R. Zhao, Z. Zhao, S. Li and W. Zhang, *J. Phys. Chem. Lett.*, 2017, **8**, 2323–2327.
55 Y. Jiang, J. Huang, W. Dai and M. Hunger, *Solid State Nucl. Magn. Reson.*, 2011, **39**, 116–141.
56 W.-H. Chen, H.-H. Ko, A. Sakthivel, S.-J. Huang, S.-H. Liu, A.-Y. Lo, T.-C. Tsai and S.-B. Liu, *Catal. Today*, 2006, **116**, 111–120.
57 W. Hu, Q. Luo, Y. Su, L. Chen, Y. Yue, C. Ye and F. Deng, *Microporous Mesoporous Mater.*, 2006, **92**, 22–30.
58 N. Feng, A. Zheng, S.-J. Huang, H. Zhang, N. Yu, C.-Y. Yang, S.-B. Liu and F. Deng, *J. Phys. Chem. C*, 2010, **114**, 15464–15472.
59 J. Huang, Y. Jiang, N. Van Vegten, M. Hunger and A. Baiker, *J. Catal.*, 2011, **281**, 352–360.
60 F. Leydier, C. Chizallet, A. Chaumonnot, M. Digne, E. Soyer, A.-A. Quoineaud, D. Costa and P. Raybaud, *J. Catal.*, 2011, **284**, 215–229.
61 M. Valla, A. J. Rossini, M. Caillot, C. Chizallet, P. Raybaud, M. Digne, A. Chaumonnot, A. Lesage, L. Emsley and J. A. Van Bokhoven, *J. Am. Chem. Soc.*, 2015, **137**, 10710–10719.
62 E. F. Rakiewicz, A. W. Peters, R. F. Wormsbecher, K. J. Sutovich and K. T. Mueller, *J. Phys. Chem. B*, 1998, **102**, 2890–2896.
63 M. D. Karra, K. J. Sutovich and K. T. Mueller, *J. Am. Chem. Soc.*, 2002, **124**, 902–903.
64 A. Zheng, L. Chen, J. Yang, M. Zhang, Y. Su, Y. Yue, C. Ye and F. Deng, *J. Phys. Chem. B*, 2005, **109**, 24273–24279.
65 S. Zhao, W. Yang, K. D. Kim, L. Wang, Z. Wang, R. Ryoo and J. Huang, *J. Phys. Chem. C*, 2021, **125**, 11665–11676.
66 X. Yi, H.-H. Ko, F. Deng, S.-B. Liu and A. Zheng, *Nat. Protoc.*, 2020, **15**, 3527–3555.
67 H. Jin, M. B. Ansari, E.-Y. Jeong and S.-E. Park, *J. Catal.*, 2012, **291**, 55–62.
68 J. Ma, W. Luo, X. Wang, X. Yu, J. J. Wang, H. Hu, H. Du, J. Zeng, W. Chen and M. Yang, *Nano-Micro Lett.*, 2026, **18**, 39.
69 M. Milina, S. Mitchell, Z. D. Trinidad, D. Verboekend and J. Pérez-Ramírez, *Catal. Sci. Technol.*, 2012, **2**, 759–766.
70 B. Yuan, Y. Li, Z. Wang, F. Yu, C. Xie and S. Yu, *Mol. Catal.*, 2017, **443**, 110–116.
71 S. Zhao, W. D. Wang, L. Wang, W. Schwieger, W. Wang and J. Huang, *ACS Catal.*, 2019, **10**, 1185–1194.